Heliyon 10 (2024) e29121

Contents lists available at ScienceDirect

Heliyon

journal homepage: www.cell.com/heliyon

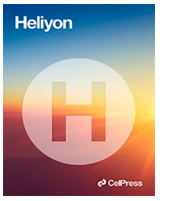

Research article

Photocatalytic activity in graded off-valent cations substituted $NaNbO_3$

Rajbala Nain, R.K. Dwivedi *

Department of Physics and Materials Science and Engineering, Jaypee Institute of Information Technology, Noida, 201309, India

A B S T R A C T

This study investigates the impact of off-valent doping on the photocatalytic properties of $NaNbO_3$ concerning the degradation of Methylene Blue. Compositions with x values of 0.00 (representing pure $NaNbO_3$, denoted as NBO) and 0.05 within the material system $Na_{1-x}A_xNbO_3$ (where A is K^{1+}, Ba^{2+}, La^{3+}, abbreviated as K-NBO, Ba-NBO, and La-NBO respectively) were synthesized using the conventional solid-state reaction method. The UV–visible analysis revealed a decrease in the band gap for samples K-NBO and Ba-NBO, while an increase was observed for sample La-NBO. Raman modes of lower wave numbers merged and shifted towards the higher wave number side. The determination of valence band edge and conduction band edge involved computational analysis based on XPS survey scans, and the band gap energy values were derived from UV–Visible spectroscopy results. Examining the band diagram of the samples (NBO, K-NBO, Ba-NBO, and La-NBO) in conjunction with the highest occupied molecular orbital and lowest unoccupied molecular orbital levels of MB dye provided insights into potential degradation mechanisms. Photocatalytic dye degradation experiments for Methylene Blue demonstrated that doping increased the degradation efficiency of samples K-NBO, Ba-NBO, and La-NBO compared to NBO. Among all $NaNbO_3$ based prepared samples, Ba-NBO exhibited the highest degradation efficiency of 96%, however slightly less than the reference sample P25 TiO_2.

1. Introduction

Industrial effluent discharge that contains organic pollutants like dye, fertiliser, or surface-active substances is transforming in a significant problem for community since they harm water streams, putting both human in addition wildlife lives at risk [1]. Globally, 0.7 million tonnes of organic harmful dyes are generated and released [2]. The main cause of water contamination is dyes and thinners used across a range of sectors, including petrochemicals, paints, textiles, agriculture and medicine, with methylene blue being the most common organic cationic dye. Some azo-dyes and their by-products, including aromatic amines, are well recognised to be very carcinogenic [3]. Through waste products from these industries, these dyes leak into the ground and pollute the source of drinking water [4]. There are numerous treatment techniques that have been established, including biological techniques, membrane separation technologies, electrochemical techniques, ozone oxidation, and others. Among these, Photocatalytic technology has great potential and feasible for treating environmental contaminants due to its high mineralization efficiency, no additional pollutants, lower consumption of energy, and simple procedures [5]. Due to its applicability in both the production of solar fuel and environmental clean-up, semiconductor photocatalysis has garnered significant and growing interest. The importance of photocatalytic wastewater clean-up and photocatalytic hydrogen production from water splitting has increased among various methods due to its environmental friendliness and water capacity for regeneration. As a result of Fujishima's ground-breaking work employing TiO_2 as a water-splitting photocatalyst, a variety of inorganic photocatalysts are now commonly being used [6]. The photocatalytic process involves various critical factors, including the bandgap energy, effective surface area, light energy absorption characteristics,

* Corresponding author
E-mail address: rk.dwivedi@jiit.ac.in (R.K. Dwivedi).

https://doi.org/10.1016/j.heliyon.2024.e29121
Received 9 January 2024; Received in revised form 29 March 2024; Accepted 1 April 2024
Available online 2 April 2024

operational intensity, temperature, and pH during the degradation process. Additionally, the bandgap energy of photocatalytic materials plays a crucial role in influencing photocatalytic activity [7].

Due to their ferroelectric and piezoelectric capabilities, niobium oxide-based perovskite-like structures, Alkali Niobate compounds, such as $LiNbO_3$, $NaNbO_3$, and $KNbO_3$, have received a lot of attention in recent years [8]. In recent times, there has been a notable surge in interest surrounding $NaNbO_3$ perovskite nanostructures, a semiconductor photocatalyst under investigation. This increased attention is attributed to their advantageous qualities, including remarkable physicochemical stability, high crystallinity, cost-effectiveness, abundance, and minimal environmental impact [9]. However, the photocatalytic activity of $NaNbO_3$ faces limitations due to its high band gap (3.4 eV) and the rapid recombination rate of photo-generated electron-hole pairs [10]. It is noteworthy that the properties and applications of $NaNbO_3$ nanoparticles are significantly influenced by their shape, size, and structure [9].

One potential approach to enhance photocatalytic activity involves introducing foreign elements through doping, aiming to modify the structural characteristics of the designated photocatalysts [6]. In a study by Jana et al. (2020), the impact of mono-doping and co-doping K and V on the dye degradation properties of $NaNbO_3$ under CFL light was investigated. The findings indicate that samples co-doped with K and V exhibited a dye degradation efficiency of 34% [11]. In a study conducted by Wu and colleagues in 2021, the influence of V doping on the degradation properties of antibiotics in $NaNbO_3$ was demonstrated. Degradation properties have been studied using tetracycline, ciprofloxacin and enrofloxacin as antibiotics. Doping of V_2O_5 has reduced the band gap to a value of 2.89 eV from 3.03 eV [12]. Li et al. (2014) studied La and Co co-doped $NaNbO_3$ for hydrogen generation. These results illustrate that the incorporation of Co introduces an additional electronic state, leading to a reduction in the band gap for enhanced absorption of visible light. The improved activity can be attributed to the Co d-d transition [13].

MB, a cationic thiazine dye, is an amorphous compound in its solid state with the chemical formula $C_{16}H_{18}N_3SCI$. The nomenclature "basic blue 9″ originates from its property of producing a dark blue-green solution, encompassing an MB cation and a chloride anion, upon dissolution in water [14]. This dye finds common applications in the dyeing processes of hemp, silk fabric, and paper [15].

Despite this, there is a notable absence of reports on A site cation doping, especially with off-valent ions, specifically for photocatalytic purposes. To address this gap, we have explored the incorporation of K^{1+}, Ba^{2+}, and La^{3+} (off-valent cations with distinct valence states) into $NaNbO_3$ with $x = 0.05$ for potential photocatalytic applications. The synthesis of these samples is carried out using the conventional solid-state reaction method. Characterization of the prepared samples involves XRD, UV, Raman, and XPS measurements. Previous studies have already highlighted the impact of off-valent substitutions on structural and electrical properties [16]. The investigation extends to the study of photocatalytic properties, specifically targeting the degradation of organic pollutants with Methylene Blue (MB) chosen as the experimental subject. This report provides a comprehensive discussion on the detailed effects of off-valent doping on the photocatalytic properties of $NaNbO_3$.

2. Experimental details

The solid-state reaction method is employed to fabricate samples within the $Na_{0.95}A_{0.05}NbO_3$ material system, where A represents K^{1+}, Ba^{2+}, and La^{3+}, abbreviated as NBO, K-NBO, Ba-NBO, and La-NBO, denoting pure, K-doped, Ba-doped, and La-doped samples, respectively. Raw materials of high purity (more than 99%), namely Na_2CO_3, Nb_2O_5, La_2O_3, K_2CO_3, and $BaCO_3$ sourced from Sigma Aldrich, are used for sample preparation. Appropriate amount of these powders are homogeneously ground in acetone media in a mortar and pestle for 4 h. Subsequently, the dried mixture undergoes calcination for 4 h at 900 °C in a tubular furnace. For the XRD characterization, a Shimadzu XRD-6000 instrument with Cu-Kα radiations (1.5406 Å) is utilized. XRD spectra for these samples have

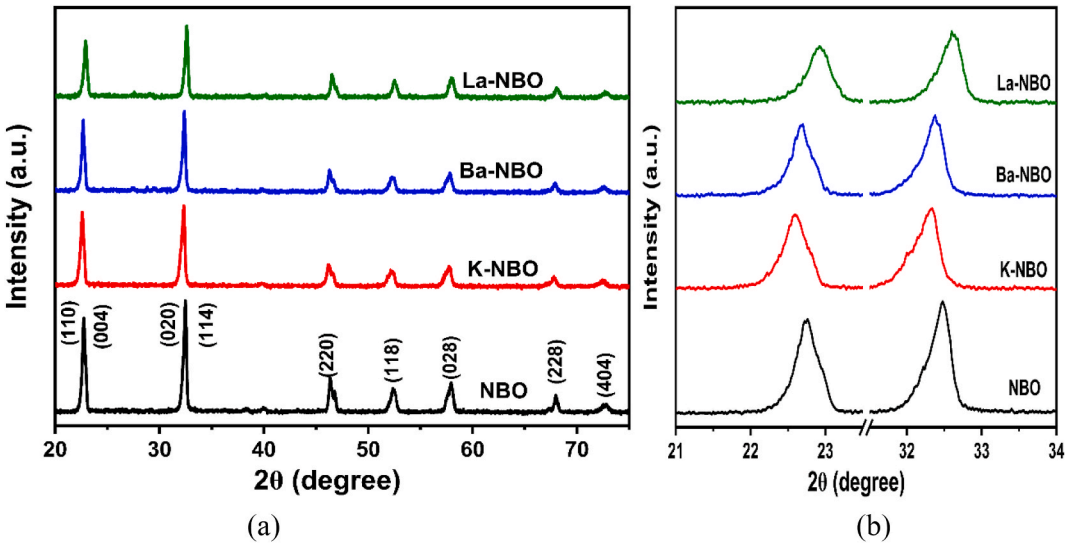

Fig. 1. (a) XRD pattern of the samples NBO, K-NBO, Ba-NBO and La-NBO (b) A closer look of the peaks within the range of $21° \leq \theta \leq 34°$.

been recorded in the 2θ range of 20°–75° with a scan speed of 2°/minute. Raman measurements are conducted using a Confocal Raman spectrometer with a laser source at 532 nm. X-ray photoelectron spectroscopy (XPS) data is acquired using an Omicron ESCA instrument by Oxford Instruments Germany. Photoluminescence spectra have been recorded using Luminescence spectrophotometer from Agilent Cary Eclipse 100 with Xenon flash lamp as source.

In order to study photocatalytic properties, the following experimental process has been adopted. Photocatalytic activity study has

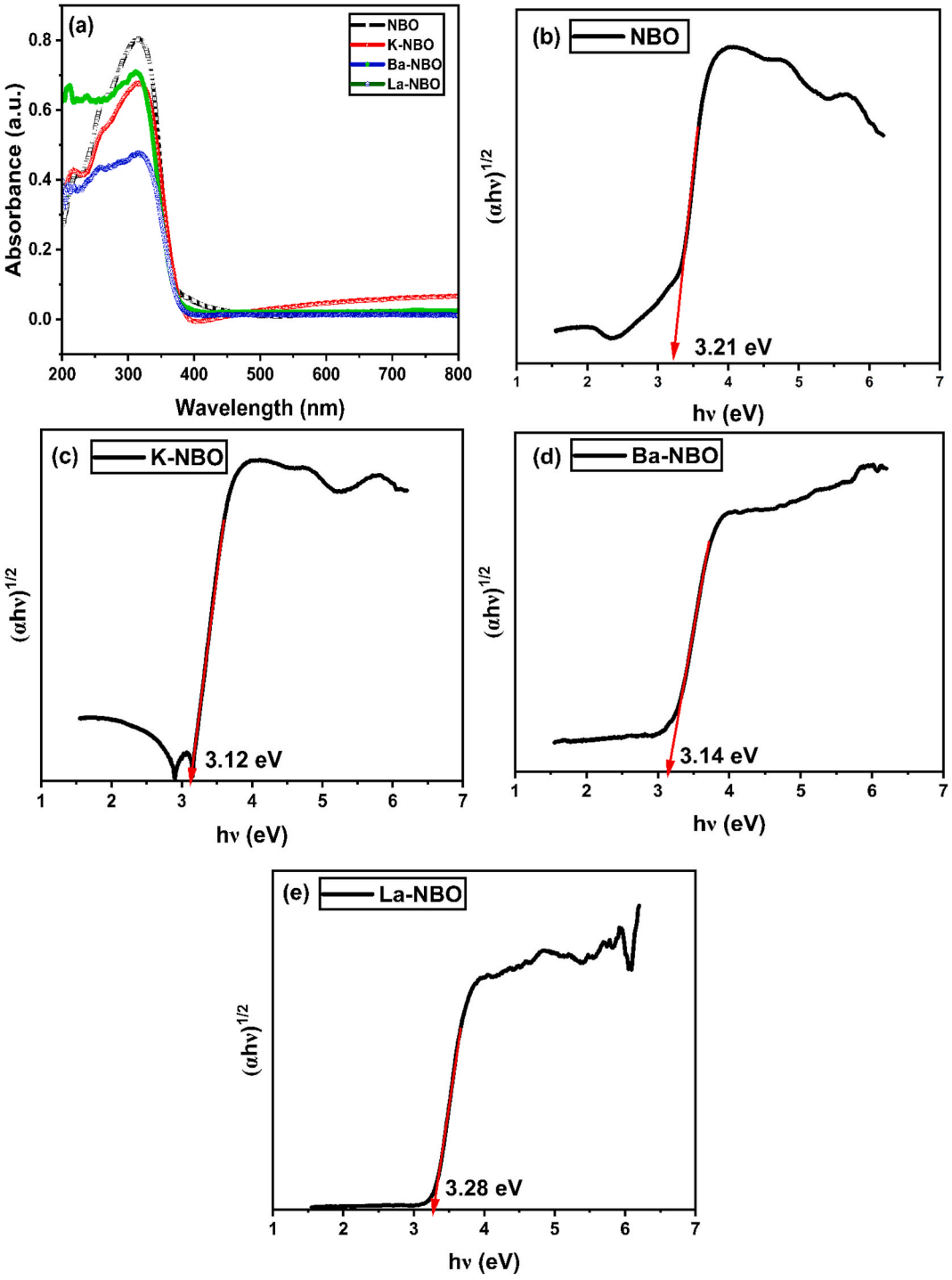

Fig. 2. (a) UV–Vis absorbance spectra for NBO, K-NBO, Ba-NBO, and La-NBO samples, coupled with Tauc plots corresponding to each sample (b) NBO, (c) K-NBO (d) Ba-NBO and (e) La-NBO.

been carried out by using a solution of methylene blue dye in distilled water. The experiment was performed in a photocatalytic reactor setup from Biogenix with a reactor of capacity of 1L with a 300W xenon lamp under full arc filter for UV irradiation. The temperature of the system was kept at 20 °C throughout the reaction with the help of a chiller. The flask's overall capacity is 1L, with the irradiated solution volume set at 100 mL. To prepare the photocatalyst solution, 20 mg of the synthesized photocatalyst is dispersed in 100 mL of a 10 ppm Methylene Blue (MB) solution. Consequently, the catalyst loading in this experiment is 0.2 g/L. Following the addition of the catalyst to the 100 mL dye solution, the resultant mixture is stirred in darkness for 30 min to allow the absorption-desorption process to attain equilibrium conditions. Subsequently, the solution is exposed to UV light, and at intervals of 30 min, 3–4 mL of the solution is collected. The absorbance spectra within the wavelength range of 500 nm–800 nm are monitored to confirm the degradation of the MB dye. This process is carried out for a duration of 3 h.

3. Results and discussion

3.1. XRD analysis

The XRD patterns of all synthesized samples are shown in Fig. 1, revealing a *Pbcm* space group symmetry with an orthorhombic structure as per the JCPDS- 073–083 data. The absence of characteristic peaks indicates the presence of the samples in a single phase. Upon doping with K and Ba, the peaks exhibit a shift towards the lower Bragg's angle side, as depicted in Fig. 1(b). Alternatively, La doping induces a peak shift for the higher Bragg's angle side. The ionic radii of the dopants, specifically K^{1+} (1.64 Å) in the K-NBO sample and Ba^{2+} (1.61 Å) in the Ba-NBO sample, surpasses the ionic radii of the host ion Na^{1+} (1.39 Å). This difference in ionic radii may accounts for the observed peak shifts and the consequent increase in interplanar spacing, leading to an enlarged unit cell size. For La-NBO samples, the XRD pattern indicates a shift towards higher angle, possibly attributed to the shorter ionic radii of La^{3+} (1.36 Å) compared to Na^{1+} (1.39 Å), resulting in a decreased interplanar spacing. The crystallite size has been determined using Scherrer formula and found to be in the range of 21 nm–36 nm which has been found to be decreased from 36 nm for pure NBO to 21 nm for La doped NBO. A comprehensive structural analysis, conducted through Rietveld refinement of diffraction data, has already been published [16].

3.2. UV–visible spectroscopy

The UV–visible spectra for the NBO, K-NBO, Ba-NBO, and La-NBO samples were recorded over the 200 nm – 800 nm wavelength range, as depicted in Fig. 2. The absorption edges for these samples are observed in the 300 nm – 350 nm range. Notably, the broad absorption band at around 300 nm is attributed to the corner-sharing NbO_6 octahedra [17]. In the UV region, NBO exhibits an absorption edge with a band gap energy of 3.21 eV, excited by the O-2p and Nb-3d states, as depicted in Fig. 2(a). The absorption edge for the doped samples has shifted towards longer wavelengths, enhancing the photocatalytic activity through increased light absorption, as indicated in Fig. 2(a) [15]. The determination of the optical band gap has been carried out using the Tauc plot, following the equation provided below:

$$(\alpha h\nu)^n = A\left(h\nu - E_g\right) \tag{1}$$

in the given context, α denotes the absorption coefficient, ν stands for light frequency, A represents the proportionality constant (band tailoring coefficient), and E_g signifies the band gap [18,19]. The 'n' parameter is dictated by the intrinsic characteristics of the materials, such as the type of transition. For materials with n = 2, they showcase direct transitions, while those with n = ½ are acknowledged for featuring indirect transitions, in accordance with equation (1) [13]. Table 1 provides an overview of the band gap values that were obtained using equation (1) and linear interpolation of $\alpha h\nu$ with $h\nu$.

The faster electron transfer at the solid-liquid interface was made achievable by the rise in band gap because it effectively separated charges, decreased the rate of electron-hole pair recombination, and increased electron separation [20]. Nevertheless, Ba-NBO exhibits superior catalytic activity in the degradation of Methylene Blue (MB), boasting a band gap energy of 3.14 eV. A smaller band gap implies a reduced energy requirement for electronic transitions, facilitating the photocatalytic process.

3.3. Raman analysis

Raman spectroscopy emerges as a valuable technique for probing the ordered a short-range arrangement of phases in perovskites. The $NaNbO_3$ exhibits an orthorhombic structure (at room temperature) identified by the *Pbcm* space group symmetry, with each unit

Table 1
Optical Band gaps of samples NBO, K-NBO, Ba-NBO and La-NBO.

Samples Name	Band Gap (eV)
NBO	3.21
K-NBO	3.12
Ba-NBO	3.14
La-NBO	3.28

cell containing eight formula units. The theoretical analysis categorizes optical vibrational modes at zero wavevector based on their irreducible representations, as outlined in equation (2):

$$\Gamma_{opt} = 15A_g + 17B_{1g} + 15B_{2g} + 13B_{3g} + 13A_u + 14B_{1u} + 16B_{2u} + 14B_{3u} \quad (2)$$

The identified Raman-active modes include A_g, B_{1g}, B_{2g}, and B_{3g} mainly, A_u remains inactive for both Raman and Infrared, while Infrared-active modes are confined to B_{1u}, B_{2u}, and B_{3u} [21]. The expected total count of Raman optical phonon modes is 60, with discernible peaks due to low intensity between specific Raman modes and accidental degeneracy. The deconvoluted Raman profile of NBO, K-NBO, Ba-NBO, and La-NBO samples at room temperature is illustrated in Fig. 3, spanning from 100 cm^{-1} to 800 cm^{-1}.

For the NBO sample, bands within the 100-1000 cm^{-1} range are linked to the internal vibrational mode of NbO_6. The band at approximately 145 cm^{-1} is attributed to NbO_6 octahedral rotational vibrations, and the wavenumber range of 150–300 cm^{-1} corresponds to the v_6 (F_{2u}) and v_5 (F_{2g}) modes, both exhibiting a triple degeneracy [22,23]. In the interval of 170 cm^{-1} to 300 cm^{-1}, the v_6 and ν_5 modes display dispersed intensity, forming a complex band profile. The faint presence of the v_4 (F_{1u}) band is observed at 379 cm^{-1} and 436 cm^{-1}. Phonon modes below 400 cm^{-1} are associated with O–Nb–O bending vibrations, while those above 400 cm^{-1} correspond to O–Nb–O stretching vibrations. The phonon modes at 569 cm^{-1} and 606 cm^{-1} are attributed to stretching vibrational symmetry ν_2 (E_g) and ν_1 (A_{1g}) (symmetric stretching) in the NbO_6 octahedron. The stretching motions include ν_1, ν_2, and ν_3, while the bending modes consist of ν_4, ν_5, and ν_6 in a perfect octahedron [24]. Among these modes, only ν_1, ν_2, and ν_5 exhibit Raman activity, with ν_3 and ν_4 being Infrared (IR) active. The triple-degenerate mode ν_6 remains silent [24]. Depending on the site symmetry, these modes may undergo splitting, and non-Raman active modes may transform into Raman active modes.

Upon doping with K, Ba, and La in NBO sample i.e. K-NBO, Ba-NBO, and La-NBO, the modes on the lower wave number side slightly merge. Additionally, the band around 436 cm^{-1} in pure $NaNbO_3$ disappears for Ba-NBO and La-NBO samples, possibly associated with disordering at A or B-sites [25]. The doping of K, Ba, and La causes the Raman modes to shift towards higher wave number side. All the modes assigned for all prepared samples have been shown in Table 2.

3.4. Photocatalytic activity study

The photocatalytic activity of the samples was studied by employing methylene blue as the model pollutant, chosen for its high

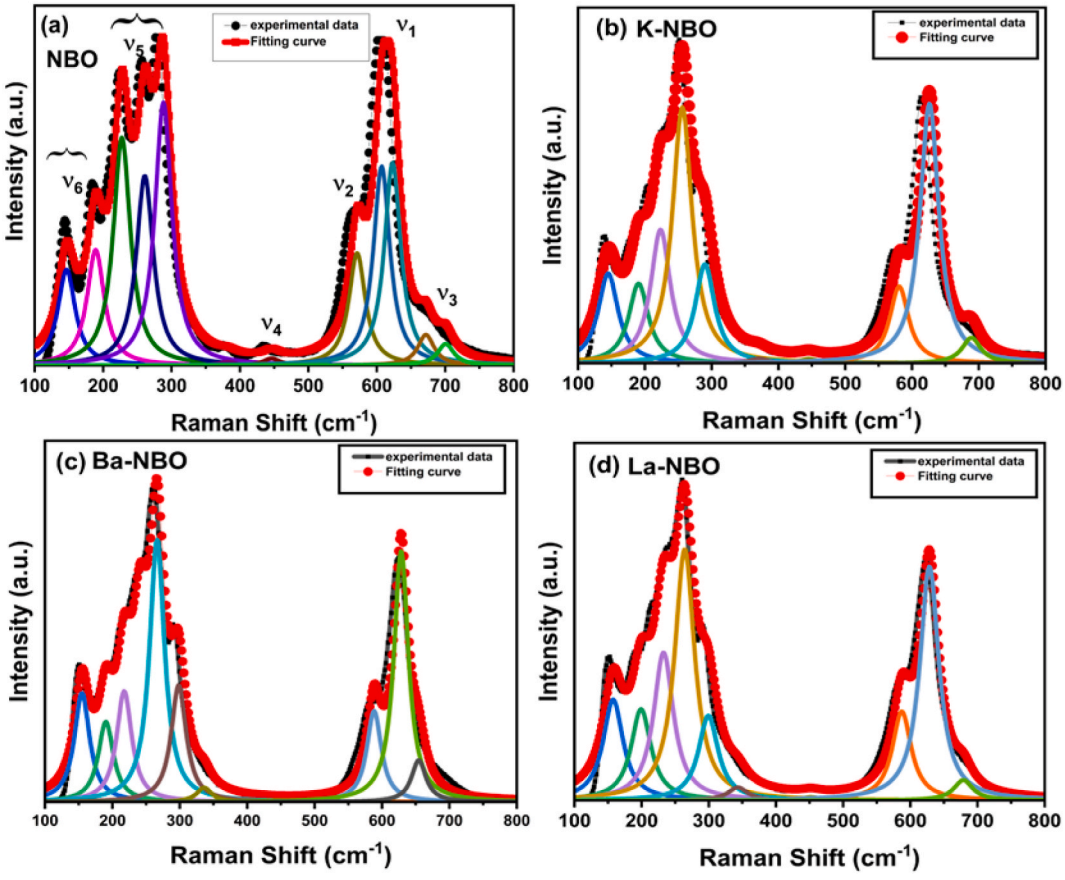

Fig. 3. Deconvoluted Raman spectra of prepared samples NBO, K-NBO, Ba-NBO and La-NBO

Table 2
Assignment of Raman modes for samples NBO, K-NBO, Ba-NBO and La-NBO.

NBO	K-NBO	Ba-NBO	La-NBO	Mode assigned
145	143	155	156	ν_6 (F_{2u})
184	189	190	198	ν_6 (F_{2u})
224	222	217	231	ν_6 (F_{2u})
257	255	265	262	ν_5(F_{2g})
280	290	298	299	ν_6 (F_{2g})
377	371	335	344	ν_4 (F_{1u})
436	445	–	–	ν_4 (F_{1u})
562	581	589	588	ν_2 (E_g)
605	626	628	629	ν_1 (A_{1g})
683	689	655	681	ν_3 (F_{1u})

stability, preventing self-degradation. In the absence of a photocatalyst, the degradation of MB dye remained stable under both light and dark conditions [26]. Furthermore, no degradation was observed in acidic and basic media, specifically in a solution with a pH of 7.00. The degradation of methylene blue occurred in the presence of UV radiation, characterized by a prominent absorption band at a wavelength of 664 nm and a shoulder at 609 nm. The primary absorption is associated with the n-π* transition, while the shoulder at 609 nm corresponds to the 0–1 vibronic transition [27].

Fig. 4 represents the decomposition of methylene blue in the presence of a catalyst for all the samples NBO, K-NBO, Ba-NBO and La-NBO. The two absorption maxima first at 609 nm and second at 664 nm of MB dye are clearly seen in all these samples. The intensity of absorption peaks at wavelengths of 609 nm and 664 nm decreases with increasing exposure time, as seen in Fig. 4(a–d). In photo decolourisation process, the major absorption edge at 664 nm decreases gradually with elapsing time. The apparent decrease the absorption band at 664 nm indicates that doped $NaNbO_3$ had initiated the photodegradation breaking the bonding in MB and decolourize the sample. From Fig. 4(a), it can be seen that absorption maxima corresponding to MB dye decrease by a very small value indicating that sample NBO shows a small degradation of MB dye. For K-NBO sample after 180 min, the absorption maxima decrease

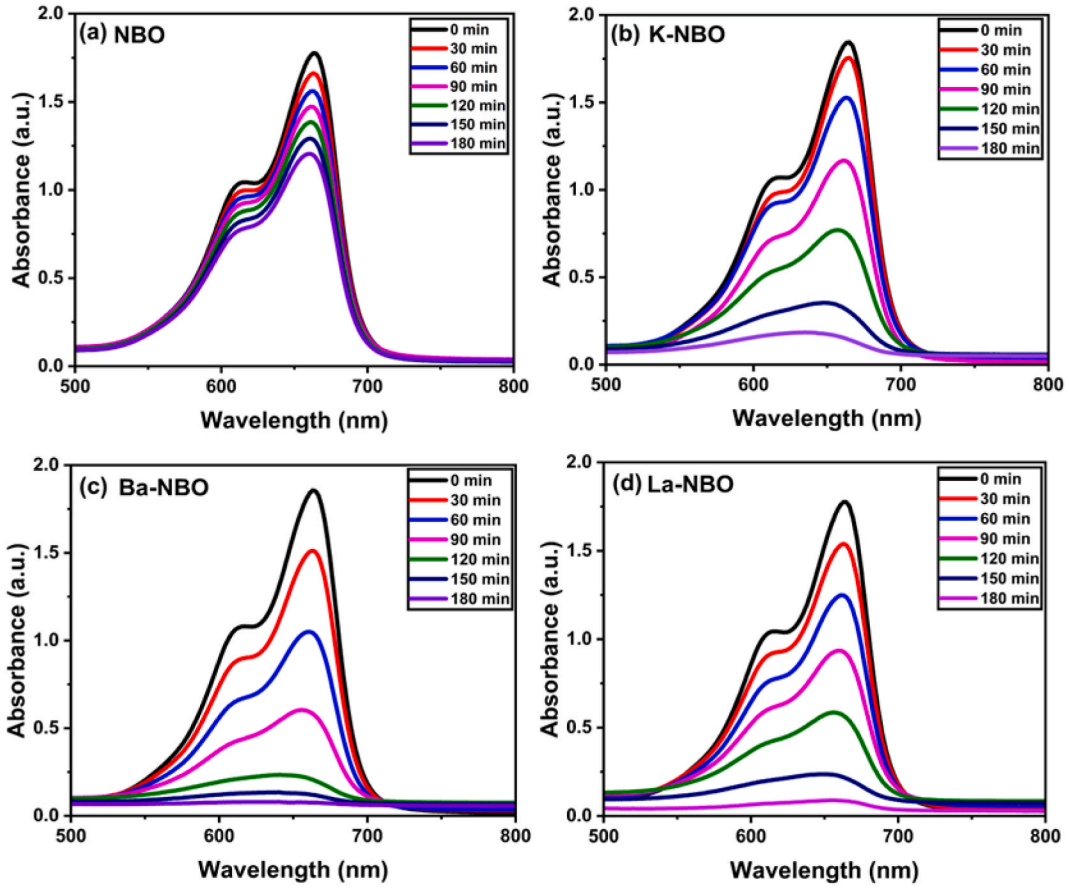

Fig. 4. Absorption spectra recorded during the photocatalytic reaction of the MB dye solution for NBO, K-NBO, Ba-NBO, and La-NBO samples.

by a large value indicates that K doped $NaNbO_3$ shows increased degradation of the MB dye. For Ba-NBO sample, the absorption peaks get smoothened after 180 min which shows the higher degradation values as compared to K-doped NBO as seen in Fig. 5 (b). For sample La-NBO degradation efficiency is higher compared to NBO and K-NBO sample but lower than Ba-NBO. The degradation efficiency is highest for Ba-NBO sample and relatively better for La-NBO sample may be due to creation of defects i.e. oxygen vacancies that are associated with the charge imbalance effect of substitution of Na by Ba and La. The generation of oxygen vacancies enhanced the delayed recombination resulting in an increased photocatalytic activity [28]. Fig. 5(a) shows the percentage degradation with time for all prepared samples. Least dye degradation is observed in pure $NaNbO_3$ which may be due to higher recombination of charge carriers under light illumination. As seen from Fig. 5(a) that Ba doped NBO shows higher degradation up to 96%. In comparison with P25 TiO_2, Ba-NBO possess slightly lower MB dye degradation efficiency. The rate constant of all the samples, determined by linear fitting, is shown in Fig. 5(b).

Several classical kinetic factors need to be considered for a more precise interpretation of the kinetic data for K, Ba, and La-doped $NaNbO_3$. The Langmuir-Hinshelwood (L-H) mechanism, which controls the kinetics of photocatalytic degradation, is widely recognised and have been used here for first order kinetics [29,30]:

$$c_t = c_0 e^{-k_1 t} \tag{3}$$

$$-\ln\left(\frac{C_t}{C_0}\right) = k_1 t \tag{4}$$

Here, C is the concentration of MB dye and k_1 is an apparent rate constant first-order reactions respectively.

The percentage degradation has been calculated by the following formula:

$$\%\ degrdation = \frac{C_0 - C_t}{C_0} \times 100 = \frac{A_0 - A_t}{A_0} \times 100 \tag{5}$$

In this context, C_0 represents the initial equilibrium concentration for absorption/desorption (at reaction time 0), while C_t stands for the concentration after reaction time t. A_0 and A_t denote the respective values of absorbance measured at 664 nm [31].

The values of degradation and rate constant are determined using the above equations which are shown in Table 3. The regression coefficient values lie close to 1 which signifies that reaction follows first order kinetics.

Cycling performance has also been tested for Ba-NBO and La-NBO samples repeatedly in different runs, shown in Fig. 6. The cycling performance for MB degradation has been tested for five cycles. In these three consecutive cycles, the performance for Ba-NBO sample was found to be 96%, 94% and 88% respectively but in 4th and 5th cycle it gets stabilized to a value of 85% (see Fig. 6a) whereas, for La-NBO sample, it was 95%, 92%, 86%, 84% and 80% respectively (see Fig. 6b). The decrease in photocatalytic performance may be due to some of the dye molecules already adsorbed on the surface of catalyst. Table 4 shows the comparative photocatalytic degradation performance of MB dye with different photocatalysts reported earlier along with this work.

3.5. XPS analysis

All these samples NBO, K-NBO, Ba-NBO and La-NBO have undergone XPS measurements to investigate the element's chemical states. These composition's spectra have been calibrated with respect to a reference carbon species, graphite, which has a binding energy of 284.6 eV. Survey scan of NBO, K-NBO, Ba-NBO and La-NBO are given in supplementary information (Figure SI-1). The sample NBO shows peaks conforming Na, Nb and O i.e the formation of $NaNbO_3$. The survey spectra of samples K-NBO, Ba-NBO and La-NBO show the presence of K, Ba and La respectively along with Na, Nb and O in these samples. Although, due to the low

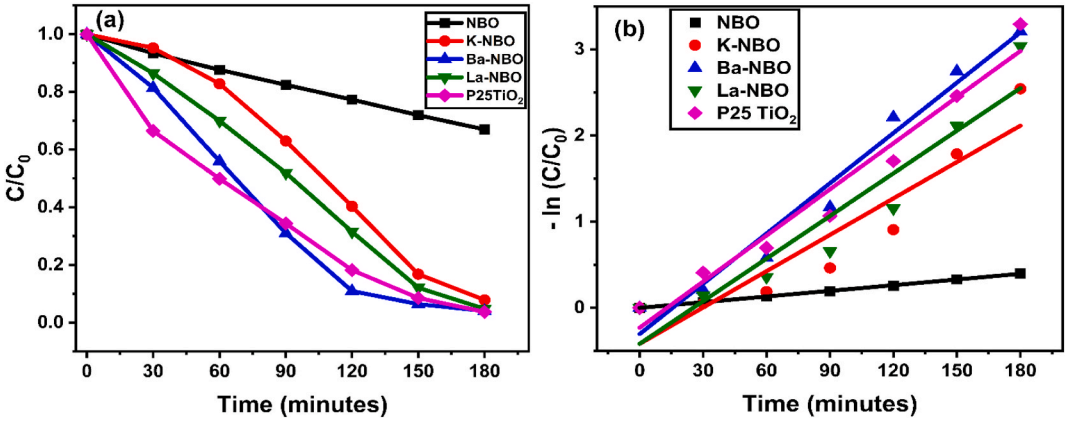

Fig. 5. (a) First order Kinetics plot for samples NBO, K-NBO, Ba-NBO, La-NBO and P25. (b) Rate constant for degradation of MB dye for samples NBO, K-NBO, Ba-NBO, La-NBO and P25 TiO_2.

Table 3
Apparent rate constant (first order) and percentage degradation of samples NBO, K-NBO, Ba-NBO, La-NBO and reference sample P25 TiO_2.

Compositions (x)	k_1 (First order) ($\pm 2 \times 10^{-3}$)	% degradation
NBO	0.003	33
K-NBO	0.014	92
Ba-NBO	0.019	96
La-NBO	0.016	95
P25 TiO_2	0.018	97

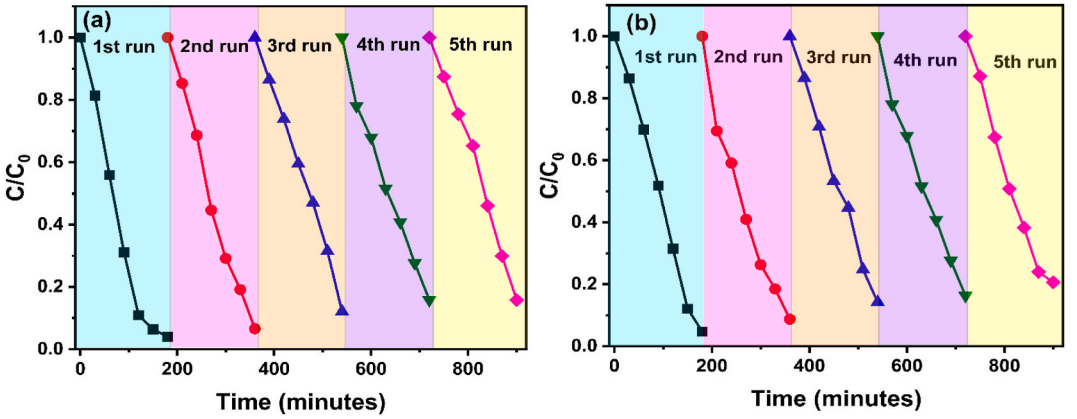

Fig. 6. Effect of cycling runs on MB degradation for catalyst (a) Ba-NBO (b) La-NBO.

Table 4
Comparative study of prepared photocatalysts for MB degradation with the reported literature.

Catalyst	Dye degraded	Light source used	Amount of catalyst used	Concentration of MB dye	Volume of MB dye	% degradation	Degradation time (minutes)	Reference
N–$SrTiO_3$	MB	Xe lamp (300W)	0.05g	10 ppm	100 mL	88	140	[2]
$NaNb_{1-x}Ta_xO_3$	MB	Xe lamp (200W)	0.02g	1×10^{-5}M	50 mLs	89	80	[6]
N–ZnO/CD	MB	UV lamp (75W)	0.05g	10 ppm	–	83.4	60	[7]
K/V– $NaNbO_3$	MB	CFL light	0.01g	10 mg/L	100 mL	34	300	[11]
Na^+ co-doped $CaTiO_3:Eu^{3+}$	MB	Mercury Lamp (35 W)	0.2g	5 mg/L	100 mL	96.62	300	[15]
La and Zr codoped $AgNbO_3$	MB	Xe lamp (300W)	0.02g	10 ppm	50 mL	48.3	300	[19]
$SrTiO_3$ @ reduced graphene oxide	MB	Halogen lamp (500W)	0.01g	100 mg/L	–	91	150	[26]
NBO	MB	Xe lamp (300W)	0.02g	10 ppm	100 mL	33	1801	Present work
K-NBO	MB	Xe lamp (300W)	0.02g	10 ppm	100 mL	92	180	Present work
Ba-NBO	MB	Xe lamp (300W)	0.02g	10 ppm	100 mL	96	180	Present work
La-NBO	MB	Xe lamp (300W)	0.02g	10 ppm	100 mL	95	180	Present work

concentration of K in the sample, the K-2p peak signal is not clear in the survey spectra of sample K-NBO but high-resolution scan show presence of Na-1s, Nb-3d, O-1s, K-2p, Ba-3d and La-3d with different oxidation states. The peak at binding energy of 1070.34 eV for sample NBO shows a singlet, indicating the +1 state of the Na atom [32]. For sample K-NBO, this Na 1s peak seems at 1071.38 eV whereas for sample Ba-NBO and La-NBO it is shifted towards a lower binding energy having values of 1071.16 eV and 1071.15 eV respectively, given in supplementary information (Figure SI-2). But in the samples K-NBO, Ba-NBO and La-NBO, the peak corresponding to Na-1s is in single form as no satellite peak is present which confirms the +1-oxidation state of Na in all these samples. Also, based on the data in the NIST XPS database, it is clear that peak associated with Na-1s is found within the range of 1070 eV–1072 eV [33].

The XPS study of p and d orbitals is difficult because of the numerous complex splits and overlapped binding energies. Fig. 7(a) shows the high-resolution scan for Na-1s for sample NBO. Fig. 7 (b) shows the high-resolution scan for K-2p for sample-NBO having binding energy spanning from 290 eV to 300 eV. The presence of two distinct peaks in the K element's binding energy, at 292.37 eV and 295.16 eV, can be attributed to the K-$2p_{3/2}$ and K-$2p_{½}$ states [34]. These two peaks show a difference of 2.79eV (~2.8eV) which signifies the K in +1 state [35]. High resolution scan for Ba-3d in sample Ba-NBO indicates the binding energy range of 775 eV–800 eV as shown in Fig. 7 (c). It is to be noted that Ba-3d shows a doublet separation of peaks $3d_{5/2}$ and $3d_{3/2}$ with the binding energy 779.293 eV and 794.637 eV respectively, which are the core lines of Ba^{2+} as reported by Yuan et al. (2018) [36]. The binding energy separation of nearly 15.34eV which is very close to 15.30 eV as reported for doublet separation of Ba-3d confirms the +2 oxidation state of Ba [33]. Fig. 7 (d) displays a detailed scan of La-3d within binding energy range of 830 eV–865 eV. The peak exhibits a segmentation into La-$3d_{5/2}$ and La-$3d_{3/2}$, characterised by four gaussian components which is in agreement with Sanvarapu et al. (2018) [37]. The main peaks at 833.9eV and 850.7eV corresponds to the spin orbit state of La-$3d_{5/2}$ and La-$3d_{3/2}$ respectively whereas the peaks at 837.9eV and 854.9eV are the satellite peaks [38]. The formation of these satellite peaks is a result of the charge transfer that occurs between the Oxygen 2p and Lanthanum 4f orbitals. The difference in binding energy between La-$3d_{5/2}$ and La-$3d_{3/2}$ is almost 16.8 eV, which is close to the 16.82 eV that has been published in the literature, which confirms the +3-oxidation state of La [39]. Additional evidence supporting the presence of La in a +3-oxidation state is the observed difference in binding energy between the La-$3d_{5/2}$ state and the satellite peak, which falls within range of 4.0 eV–4.6 eV as reported in the literature. Furthermore, the ratio of the peak area surpassing unity serves as additional confirmation for the existence of La in the +3 oxidation state.

The core level with $l \geq 1$ appears as spin doublets as a result of spin orbit interactions. The core spectrum for the Nb-3d level in sample NBO reveals a doublet, with binding energies of 209.01 eV and 206.27 eV for Nb-$3d_{3/2}$ and Nb-$3d_{5/2}$, respectively as shown in Fig. 8(a). The peaks exhibit a Binding energy difference of 2.74 eV and a branching ratio of 1.7, which closely aligns with the value of 1.5 reported in literature [33]. The indication of Niobium in the +5 oxidation state is derived from a discernible difference in binding energy of 2.74eV and the absence of any satellite peak observed in the NBO sample. But, for samples K-NBO, Ba-NBO and La-NBO, there is an extra shoulder present at lower binding energy nearly at 205 eV. The high-resolution scan of Nb-3d for samples K-NBO, Ba-NBO and La-NBO have been deconvolved into four peaks with +4 and + 5 oxidation states of Nb-3d as shown in Fig. 8 (b, c, d). For sample K-NBO, the peaks corresponding to Nb^{5+} states appear at the binding energy of 206.36 eV and 209.13 eV corresponding to

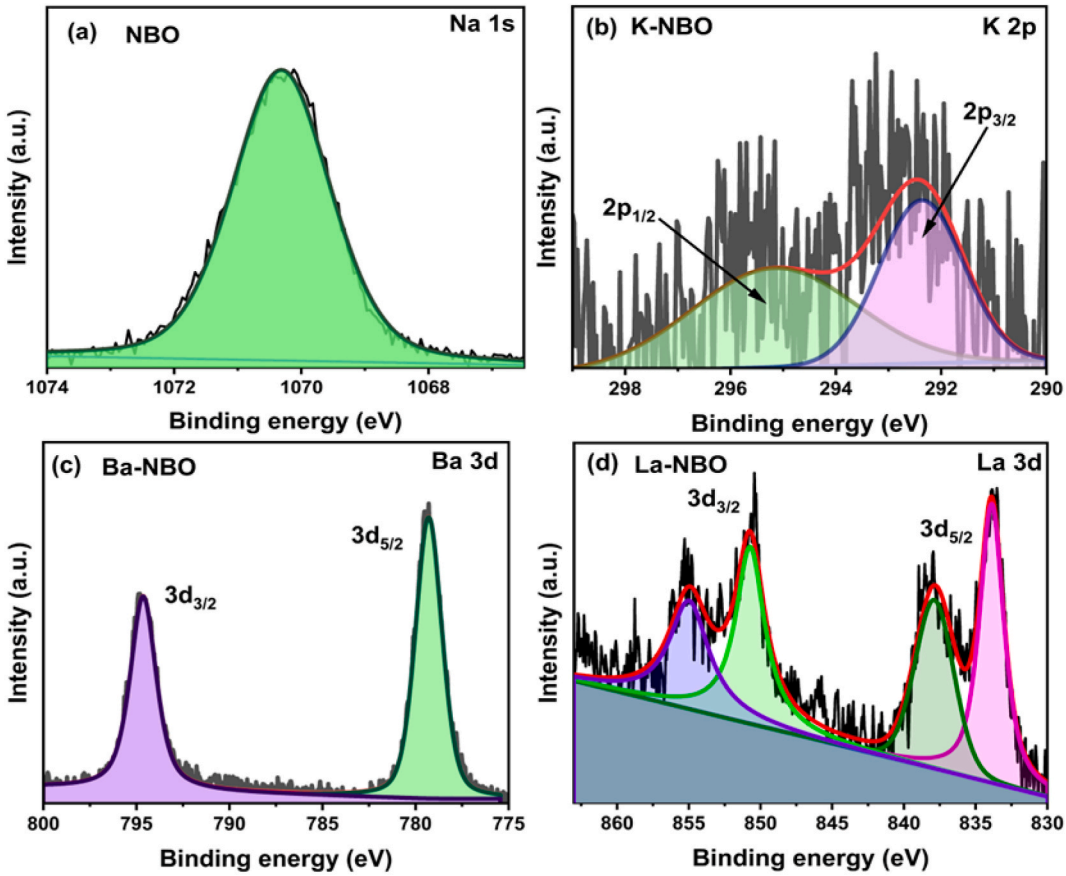

Fig. 7. (a) High resolution scan of Na-1s in sample NBO (b) High resolution scan of K-2p in sample K-NBO (c) High resolution scan of Ba-3d in sample Ba-NBO (d) High resolution scan of La-3d in sample La-NBO.

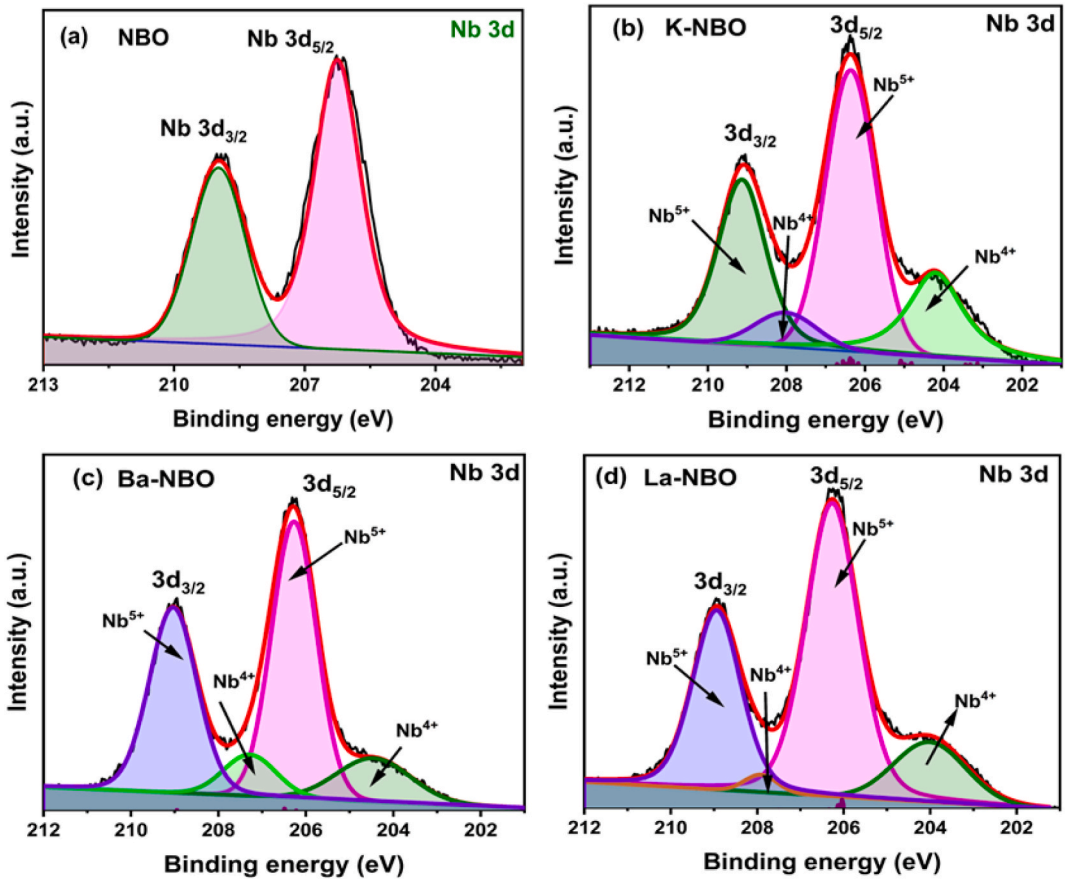

Fig. 8. (a) High resolution scan of Nb-3d in sample NBO (b) High resolution scan of Nb-3d in sample K-NBO (c) High resolution scan of Nb-3d in sample Ba-NBO (d) High resolution scan of Nb-3d in sample La-NBO.

$3d_{5/2}$ and $3d_{3/2}$ states with a binding energy separation of ~2.77eV which confirms the +5 oxidation states of Nb [40,41]. The peaks appearing around 204.21eV and 208.01 eV with a slight shift in binding energy due to K doping corresponds to Nb^{4+} states as reported in literature [42,43]. For sample Ba-NBO, Nb-3d spectrum have been shown in Fig. 8 (c). In this sample, the peaks appearing at binding energies of 206.27 eV and 209.04 eV correspond to +5 state of Nb and the peaks appearing at 205.45 eV and 207.28 eV are attributed to +4 oxidation state of Nb. In sample La-NBO, as shown in Fig. 8 (d), the peaks arising at 208.94 eV and 206.26 eV are due to +5 and the peaks appearing at 204.01eV and 207.92eV are due to +4 oxidation state of Niobium atom. The high-resolution spectra of Nb for different samples NBO, K-NBO, Ba-NBO and La-NBO suggest that doping of K, Ba and La not only introduces the extra oxidation state of Nb (+4) in the system but also shifts the binding energy towards the lower side. Thus, it is concluded from XPS spectra that the doping of K, Ba and La may create Nb^{4+} in addition to Nb^{5+} in these samples which may be caused by charge compensation internally in these materials systems [44].

Fig. 9 (a, b, c, d) shows the Oxygen 1s (O-1s) spectra for NBO, K-NBO, Ba-NBO and La-NBO samples. The whole spectrum of all these samples have been modelled into three gaussian peaks, as shown in Fig. 9 as per Yang et al. (2019) [45]. The peak around 529.07 eV resembles to the oxygen at lattice (O_L) in the perovskite structure, Oxygen vacancies are represented by peaks at 530.60 eV, and chemisorbed oxygen dissociated oxygen or water is depicted by peaks at 533.05 eV, according to Ye et al. (2022). The ratio of the peak oxygen vacancy area to the oxygen connected to lattice sites can be used to determine the relative number of oxygen vacancies, O_V/O_L which is given in the Table 5. Widely acknowledged, the charge transporters in oxide semiconductors are typically associated with the presence of oxygen vacancies, as depicted below:

$$O_O = \frac{1}{2}O_2(g) + V_O^{**} + 2e^- \tag{6}$$

The O 1s peak, which is centred at a binding energy of approximately 529.03 eV, provides confirmation of the existence of oxygen in the system with a -2-oxidation state.

It can be clearly understood from Fig. 9 that the oxygen vacancy area is less in sample NBO (7.3%), which increases in sample K-NBO (13.5 %). For Ba and La doped samples i.e. Ba-NBO and La-NBO the oxygen vacancy area is increased i.e 18.2% for sample Ba-NBO and 23.3% for sample La-NBO. This may be due to creation of a larger number of oxygen vacancies for the charge compensation of

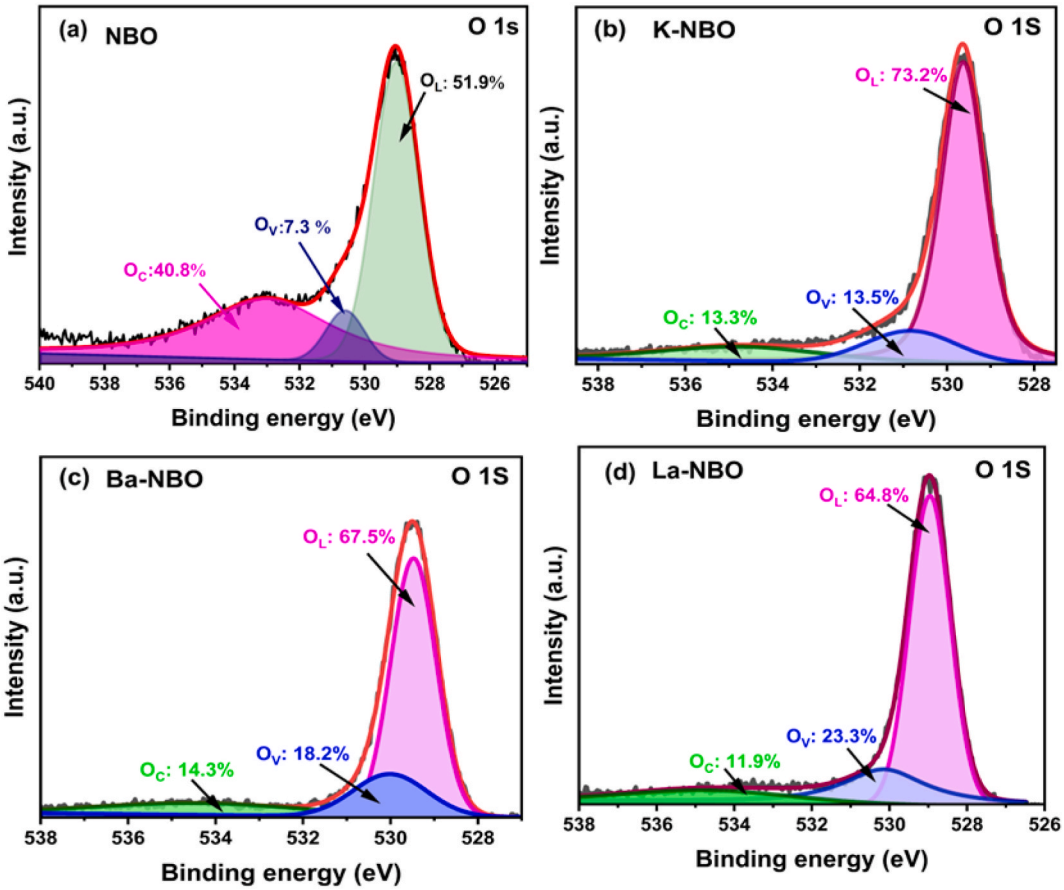

Fig. 9. XPS profile of O-1s peaks for samples (a) NBO, (b) K-NBO, (c) Ba-NBO and (d) La-NBO.

Table 5
Parameters related to O_V, O_L, and their respective ratios in the XPS profiles for the K-NBO, Ba-NBO, and La-NBO samples.

Sample Name	O_V	O_L	O_V/O_L
NBO	0.073	0.519	0.141
K-NBO	0.135	0.732	0.184
Ba-NBO	0.182	0.675	0.270
La-NBO	0.233	0.648	0.360

off valent doping of ions at the Na site.

4. Energy level diagram and possible degradation mechanism

Due to the presence of NbO_6 octahedral chains, which potentially enhance the likelihood of charge carrier delocalization during the catalytic reaction, one can infer that perovskite catalysts based on $NaNbO_3$ demonstrate noteworthy photocatalytic activity in dye degradation when exposed to sunlight. The reaction encompasses four primary steps, outlined below:

(1) Absorption of light by catalyst that produces an electron-hole pair
(2) Separation of excited charges (e^-- h^+)
(3) Transfer of electron and holes to the surface of catalyst
(4) Surface desorption and diffusion of pollutants from catalyst

The positions of the valence band and conduction band edges of the catalyst were computed, and their alignment concerning the potential of $OH^\bullet/H_2O$, $O_2/O_2^{\bullet-}$, and HOMO-LUMO levels of methylene blue dye were analyzed. This analysis aimed to gain insights into the photocatalytic activity of the catalyst, involving the separation of photogenerated electrons and holes. Valence band spectra were

acquired for each sample to determine electronic transitions. Specifically, the valence band edge (VBE) positions were identified at 2.10 eV, 2.32 eV, 2.45 eV, and 2.28 eV for samples NBO, K-NBO, Ba-NBO, and La-NBO, respectively, with reference to binding energy (eV) (refer to supplementary information, SI-3). Considering the XPS instrument's work function of 4.5 eV, the valence band positions were referenced to NHE, assuming 4.5 eV in vacuum is 0 eV w.r.t. NHE [46]. Based on the optical band gap energy (E_g), the conduction band edge (CBE) was calculated, resulting in values of −1.11 eV, −0.80 eV, −0.69 eV, and −1.00 eV for samples NBO, K-NBO, Ba-NBO, and La-NBO, respectively (CBE = VBE - E_g) [11]. During the light illumination, photon-matter interaction occurred, generating electron and hole pairs in the valence and conduction bands, respectively. Utilizing the calculated values, a band diagram was constructed concerning the HOMO and LUMO levels of MB dye. The HOMO and LUMO levels of MB dye, set at −0.88 eV and 1.55 eV, respectively, were employed to create the band diagram [47]. Redox potential values for $O_2/O_2^{\bullet-}$ (−0.33 eV vs. NHE), O_2/H_2O_2 (0.685 eV vs. NHE), $OH/OH^{\bullet}$ (1.99 eV vs. NHE), and OH/H_2O (2.70 eV vs. NHE) were extracted from the literature [48]. The calculated values of CBE and VBE edges are summarized in Table 6.

The photogenerated electrons in the semiconductor conduction band (samples NBO, K-NBO, Ba-NBO, and La-NBO a) are capable of reducing dissolved O_2 to produce the $O_2^{\bullet-}$ radical since the conduction band (−1.11 eV, −0.80 eV, −0.69 eV, and −1.00 eV) has a higher energy level than the redox potential of E (O_2/O_2•-) (eq. (3)). Consequently, superoxide ions play a role in the degradation mechanism. Additionally, the more negative conduction band edge potential compared to the standard redox potential of E (O_2/H_2O_2) suggests that oxygen absorbed on the surface of samples can react with electrons, forming H_2O_2, which further decomposes into OH radicals (eqs. (13) and (14)). The valence band potential of samples (NBO, K-NBO, and Ba-NBO) is more positive than the standard redox potential of (OH/OH^-), indicating that holes in the valence band can oxidize OH^- to $OH^{\bullet}$. Through this mechanism, holes can either directly attack the dye for mineralization or absorb water to form hydroxyl radicals (eqs. (11) and (16)). Consequently, holes emerge as the major active species driving the degradation mechanism.

It is essential for the conduction band edge position of the $NaNbO_3$ semiconductor to be lower than the lowest unoccupied molecular orbital of the MB dye to facilitate successful electron transfer during photo-assisted oxidation [49]. Additionally, having the valence band position below the HOMO level of the MB dye promotes the transfer of holes (h^+) from the photocatalyst to the adsorbed dye molecule, leading to efficient dye degradation [50].

In the case of samples NBO and K-NBO, photocatalytic degradation occurs through the excitation of electrons from the valence band to the conduction band. These generated electrons are exclusively involved in the production of $O_2^{\bullet-}$, which reacts with dye molecules, leading to the formation of degraded products. In this context, electrons from the LUMO level of the dye cannot transfer to the conduction band of the catalyst due to a higher potential. For samples K-NBO and Ba-NBO, a photosensitized mechanism (sensitization-mediated photocatalytic degradation) or a photo-assisted mechanism takes place. This occurs when sub-band light is utilized, causing the dye molecule to become excited, leading to the injection of carriers (usually electrons) followed by interfacial charge transfer. Such a mechanism is only effective when the semiconductor conduction band edge is below the dye molecule's LUMO level. Based on the positions of the valence band and conduction band obtained from XPS and the HOMO-LUMO levels of MB dye, an energy level diagram illustrating the possible degradation has been depicted and is presented in Figs. 10 and 11 for samples NBO, K-NBO, Ba-NBO, and La-NBO.

4.1. Scavenger test

For the confirmation of active species involved in the reaction, scavenger test has been carried out for Ba-NBO sample (showing maximum efficiency) using EDTA, *p*-benzoquinone (BQ) and Isopropyl alcohol (IPA) which are trapping agents of holes (h^+), $O_2^{-\bullet}$ and $^{\bullet}OH$ respectively [32]. Fig. 12 shows the degradation of MB dye without scavenger and with EDTA, BQ and IPA. It can be seen that in absence of any scavenger, no effect is observed on photocatalytic degradation of Ba-NBO. It is found that in presence of *p*-benzoquinone and Isopropyl alcohol, photocatalytic performance reduces to 72% and 66% respectively. Further, with the addition of EDTA to the solution, an abrupt decrease in the degradation efficiency to 25% is observed. It is therefore inferred from these observations that holes are the major active species and $O_2^{-\bullet}$ and $^{\bullet}OH$ radicals have a little contribution in photodegradation process (see Fig. 13).

5. Discussion

It is to mention that the defect chemistry plays an important role not only to influence the structural and electrical behaviour but also the photocatalytic properties. In recent years, NBO has shown its ability to degrade hazardous dyes such as rhodamine B and MB dye from polluted water. The effect of substitution of K^{1+}, Ba^{2+} and La^{3+} at Na^{1+} site in NBO lattice has also been studied on photocatalytic properties of these materials. It has been observed that off-valent dopants contribute to the creation of additional charge defects, ensuring an overall charge imbalance in the samples, as outlined below [16].:

Table 6
Valence band and conduction band positions calculated for samples NBO, K-NBO, Ba-NBO and La-NBO

Sample Name	Band Gap (eV)	Valence band (eV)	Conduction band (eV)
NBO	3.21	2.10	−1.11
K-NBO	3.12	2.32	−0.80
Ba-NBO	3.14	2.45	−0.69
La-NBO	3.28	2.28	−1.00

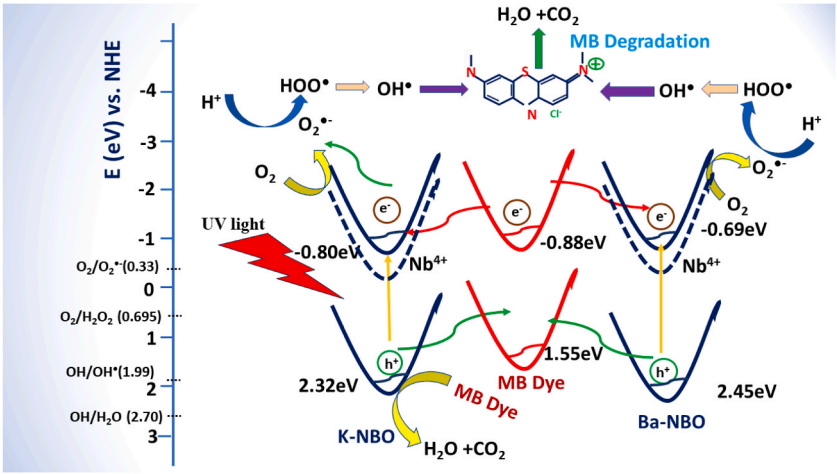

Fig. 10. Diagrammatic depiction of possible photocatalytic breakdown process for samples K-NBO and Ba-NBO.

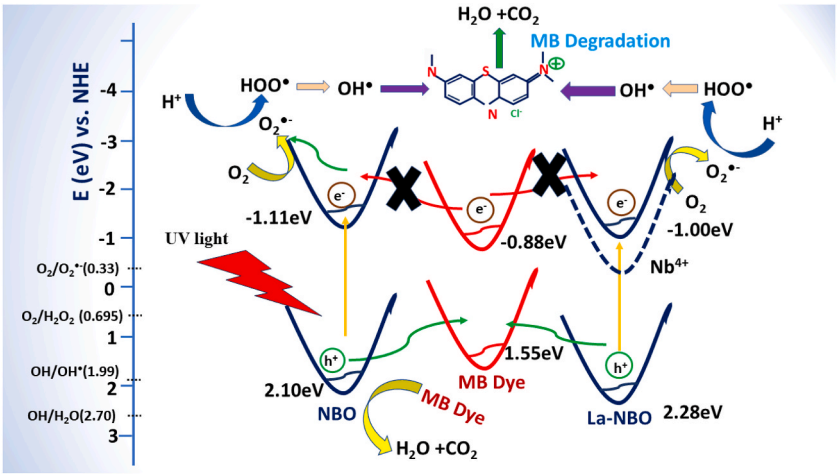

Fig. 11. Diagrammatic depiction of possible photocatalytic breakdown process for samples NBO and La-NBO.

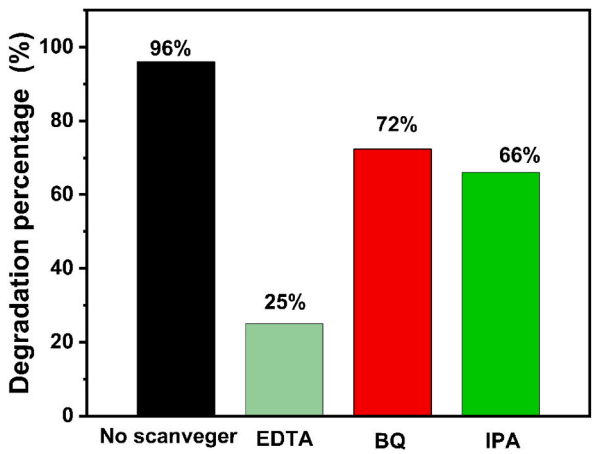

Fig. 12. Photocatalytic degradation of MB dye for Ba-NBO sample with scavenger and without scavenger.

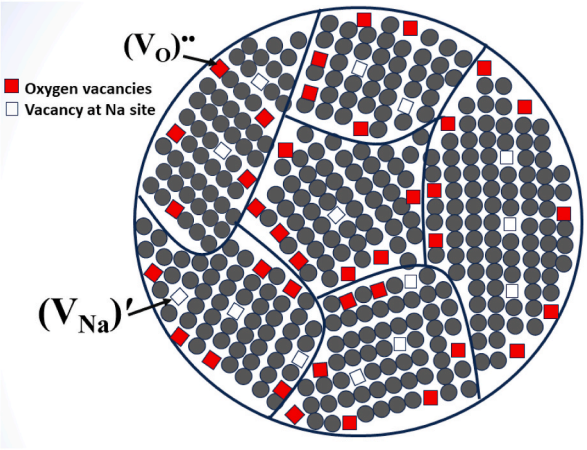

Fig. 13. Occurrence of defects like $(V_{Na})'$ and $(V_O)^{\bullet\bullet}$ in the bulk as well at the surfaces.

$$Ba_{Na} \rightarrow (Ba_{Na})^{\bullet} + (V_{Na}^{1+})' \ldots \quad (7)$$

$$La_{Na} \rightarrow (La_{Na})^{\bullet\bullet} + 2(V_{Na}^{1+})' \ldots \quad (8)$$

It is understood that while K^{1+} is replaced by Na^{1+}, there is no possiblity of creation of defects due to isovalent substituitions, but due to offvalent substituitions like Ba^{2+} and La^{3+}, the evident formation of defects, as described by equations (7) and (8) is crucial to maintaining overall charge neutrality in the material. Usually, such defects like $(V_{Na})'$ due to Ba^{2+}, and 2 $(V_{Na})'$ due to La^{3+} occur at regular lattice sites which may be in the bulk and at the surfaces as well i.e. at the grainboundaries as shown in the Fig. 13.

In addition to this, as it is also known that at higher temperatures during heating, oxygen evaporates in general from oxides, resulting in creation of positively charged oxygen vacancies associated with electrons as as per equation (9) below.

$$O_O = 1/2O_2 + V_O^{\bullet\bullet} + 2e^{'} \quad (9)$$

While cooling, these doubly ionized oxygen vacancies ($V_O^{\bullet\bullet}$) are transformed into singly ionized oxygen vacancies $(V_O)^{\bullet}$ as below:

$$V_O^{\bullet\bullet} + e^{-} \rightarrow V_O^{\bullet} \quad (10)$$

Usually, these oxygen vacancies occur at the grain boundaries or surfaces. In this process, positive charge defects and electrons are generated. As per the Table 3, for NBO sample the degradation efficiency is 33% (pure NBO), which is increased significantly to 92% for K-NBO, 96% for Ba-NBO and 95% for La-NBO respectively for K, Ba and La doped NBO samples. For Ba-NBO and La-NBO, the extrinsic defects are created according to equations (7) and (8) whereas for K-NBO, no such defects are created, even degradation efficiency is high enough for this samples (K-NBO). This led to an understanding that defects created by off-valent doping do not contribute to photocatalytic activity directly but caused by oxygen vacancies due to charge imbalance inside the materials and hence, increased dye degradation efficiency may be majorly caused by oxygen vacancies as evidenced by XPS which capture photogenerated electron-hole pair resulting in less recombination. Moreover, the abundance of O_2^- species throughout the lattice establishes O-2p holes in the outer orbit of O. These vacancies may generate additional defect sites which contribute to electronic transitions, eventually leading to a delay in recombination during photochemical reactions [51].

Further, when light interacts with matter (powders of pure and modified NBO), the holes are generated in valence band and electrons are generated in conduction band as below [52]:

$$\text{Doped } NaNbO_3 + h\nu \rightarrow \text{doped } NaNbO_3\ (h^{+}{}_{VB} + e^{-}{}_{CB}) \quad (11)$$

When the powders of these samples are dispersed in industrial waste water containing MB dye and light is incident on it. The $OH^{\bullet}$ and $O_2^{-\bullet}$ radicals are formed at the surface of catalyst as per the following reactions:

$$H_2O\ (ads) + (h^{+}{}_{VB}) \rightarrow OH^{\bullet}\ (ads) + H^{+}\ (ads) \quad (12)$$

$$O_2 + (e^{-}{}_{CB}) \rightarrow O_2^{-\bullet}\ (ads) \quad (13)$$

$$O_2\ (ads) + 2H^{+} + 2e\text{-} \rightarrow H_2O_2 \quad (14)$$

$$H_2O_2 + e- \rightarrow 2\ OH^{\bullet} \quad (15)$$

$$\text{MB dye} + OH^{\bullet} \rightarrow CO_2 + H_2O \quad (16)$$

Thus, generated electrons and holes may directly react with MB dye to produce degraded product as below:

$$\text{Dye} + h^{+}\ (\text{VB}) \rightarrow \text{Oxidation products } (CO_2 + H_2O) \quad (17)$$

$$\text{Dye} + e^{-}\ (\text{CB}) \rightarrow \text{Reduction products } (CO_2 + H_2O) \quad (18)$$

It is further pointed out that impedance spectroscopy of these samples at room temperature has revealed that resistance for sample NBO is highest 215.60 MΩ and Ba-NBO is lowest 2.10 MΩ (See supplimentary information, Figure.SI-4) which witnesses that recomination for NBO is more and less for Ba-NBO, resulting in lower photocatalytic activity for NBO and maximum photocatalytic degradation for Ba-NBO. Moreover, in the cases of K-NBO, Ba-NBO, and La-NBO samples, the enhanced photocatalytic efficiency can be attributed to the generation of an additional electronic state of Nb^{4+} (as indicated by XPS), situated between the valence and conduction bands. This newly created state serves as an active centre for electron capture, effectively impeding the recombination of electron-hole pairs [11].

Charge separation and recombination rate of electron-hole pair plays a crucial role in photocatalytic reaction which has been studied using photoluminescence spectroscopy (PL). It can be seen from Fig. 14 that NBO sample have maximum intensity and doped NBO samples show a decrease in intensity. According to Yang et al. (2019), intensity of PL spectra is related to the recombination of electron-hole pair [45]. Lower value of PL intensity signifies the faster charge separation whereas, a higher PL intensity corresponds to the lower charge separation i.e. faster recombination of photogenerated electron-hole pair. The least intensity of Ba-NBO sample indicates the faster charge separation, resulting in maximum efficiency for MB dye degradation whereas NBO shows minimum efficiency which may be due to faster electron-hole recombination.

6. Conclusion

The XRD patterns for all compositions reveal the formation of a single phase. Raman modes of $NaNbO_3$ demonstrate a shift towards higher wave numbers in K, Ba, and La-doped NBO samples. XPS spectra confirm the presence of additional Nb^{4+} ions alongside Na^{1+}, K^{1+}, Nb^{5+}, and O^{2-} ionic states. Ba and La-doped NBO samples exhibit notable MB dye degradation efficiencies of 96% and 95%, respectively, under UV light illumination. This enhanced efficiency may be attributed to the presence of oxygen vacancies ($V_O^{\bullet\bullet}$) and holes (h^{+}) acting as an electron-capturing entity on the photocatalytic material's surface. Furthermore, the potential contribution of Nb^{4+} ionic states, confirmed from XPS spectra, near the conduction band edge cannot be ignored as a factor for high photocatalytic response. These findings collectively contribute to a comprehensive understanding of the photocatalytic properties of the doped $NaNbO_3$ materials.

CRediT authorship contribution statement

Rajbala Nain: Writing – original draft, Validation, Investigation, Formal analysis, Data curation. **R.K. Dwivedi:** Writing – review & editing, Supervision, Conceptualization.

Declaration of competing interest

The authors declare the following financial interests/personal relationships which may be considered as potential competing interests:Rajbala Nain reports equipment, drugs, or supplies was provided by Deenbandhu Chhotu Ram University of Science and

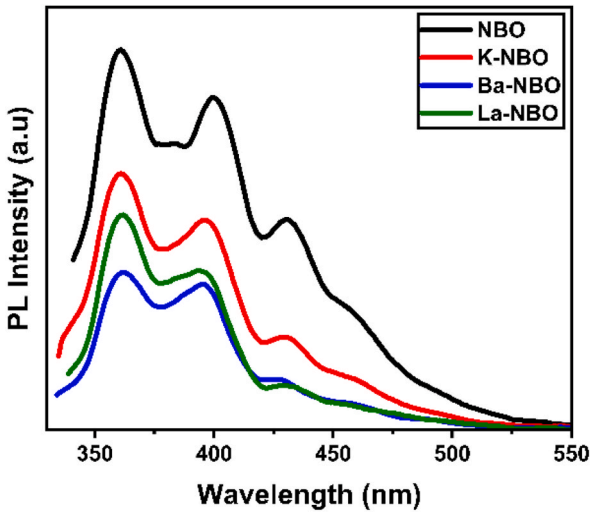

Fig. 14. Photoluminescence spectra of NBO, K-NBO, Ba-NBO, and La-NBO samples.

Technology.

Acknowledgment

Ms. Rajbala Nain expresses sincere appreciation for the Senior Research Fellowship awarded by UGC. The author extends gratitude to the Department of Physics at IIT BHU for facilitating UV absorbance measurements. Additionally, acknowledgment is extended to MNIT, MRC Jaipur, for assistance with Raman and XPS measurements, and the Department of Chemistry at DCRUST, Murthal, for support in conducting photocatalytic activity measurements.

Appendix A. Supplementary data

Supplementary data to this article can be found online at https://doi.org/10.1016/j.heliyon.2024.e29121.

References

[1] Y. Cui, et al., Effect of ferroelectricity on solar-light-driven photocatalytic activity of $BaTiO_3$- influence on the carrier separation and stern layer formation, Chem. Mater. 118 (2021) 1–10, https://doi.org/10.1021/cm402092f.
[2] Q.I. Rahman, et al., Synthesis and characterizations of nitrogen (N) doped strontium titanate ($SrTiO_3$) nanoparticles for enhanced visible light driven photocatalytic degradation, J. Nanosci. Nanotechnol. 20 (2020) 6475–6481, https://doi.org/10.1166/jnn.2020.18591.
[3] H. Lachheb, et al., Photocatalytic degradation of various types of dyes (alizarin S, crocein orange G, methyl red, Congo red, methylene blue) in water by UV-irradiated titania, Appl. Catal. B Environ. 39 (2002) 75–90, https://doi.org/10.1016/S0926-3373(02)00078-4.
[4] N. Muhd Julkapli, S. Bagheri, S. Bee Abd Hamid, Recent advances in heterogeneous photocatalytic decolorization of synthetic dyes, Sci. World J. 2014 (2014) 1–25, https://doi.org/10.1155/2014/692307.
[5] J. Li, et al., Visible-light photocatalytic performance, recovery and degradation mechanism of ternary magnetic Fe 3 O 4/BiOBr/BiOI composite, RSC Adv. 9 (2019) 23545–23553, https://doi.org/10.1039/C9RA04412D.
[6] U. Farooq, J. Ahmed, S.M. Alshehri, Y. Mao, T. Ahmad, Self-assembled interwoven nanohierarchitectures of NaNbO 3 and $NaNb_{1-x}Ta_xO_3$ ($0.05 \leq x \leq 0.20$): synthesis, structural characterization, photocatalytic applications, and dielectric properties, ACS Omega 7 (2022) 16952–16967, https://doi.org/10.1021/acsomega.1c07250.
[7] D.G. Ayu, et al., Photocatalytic degradation of methylene blue using N-doped ZnO/carbon dot (N-ZnO/CD) nanocomposites derived from organic soybean, ACS Omega 8 (2023) 14965–14984, https://doi.org/10.1021/acsomega.2c07546.
[8] F.R. Praxedes, M.A.L. Nobre, P.S. Poon, J. Matos, S. Lanfredi, Nanostructured $K_xNa_{1-x}NbO_3$ hollow spheres as potential materials for the photocatalytic treatment of polluted water, Appl. Catal. B Environ. 298 (2021) 120502, https://doi.org/10.1016/j.apcatb.2021.120502.
[9] A. Sharma, U. Bhardwaj, D. Jain, H.S. Kushwaha, $NaNbO_3$ nanorods: photopiezocatalysts for elevated bacterial disinfection and wastewater treatment, ACS Omega 7 (2022) 7595–7605, https://doi.org/10.1021/acsomega.1c06109.
[10] F. Yang, et al., Embedding Pt nanoparticles at the interface of CdS/$NaNbO_3$ nanorods heterojunction with bridge design for superior Z-Scheme photocatalytic hydrogen evolution, Appl. Catal. B Environ. 278 (2020) 119290, https://doi.org/10.1016/j.apcatb.2020.119290.
[11] R. Jana, A. Gupta, R. Choudhary, O.P. Pandey, Influence of cationic doping at different sites in $NaNbO_3$ on the photocatalytic degradation of methylene blue dye, J. Sol. Gel Sci. Technol. 96 (2020) 405–415, https://doi.org/10.1007/s10971-020-05365-1.
[12] J. Wu, et al., Study on the performance of vanadium doped $NaNbO_3$ photocatalyst degradation antibiotics, Inorg. Chem. Commun. 108669 (2021), https://doi.org/10.1016/j.inoche.2021.108669.
[13] P. Li, H. Abe, J. Ye, Band-gap engineering of $NaNbO_3$ for photocatalytic H 2 evolution with visible light, Int. J. Photoenergy 2014 (2014) 1–6, https://doi.org/10.1155/2014/380421.
[14] P. Temeepresertkij, M. Iwaoka, S. Iwamori, Molecular interactions between methylene blue and sodium alginate studied by molecular orbital calculations, Molecules 26 (2021) 1–7, https://doi.org/10.3390/molecules26227029.
[15] M. Chen, Q. Xiong, Z. Liu, K. Qiu, X. Xiao, Synthesis and photocatalytic activity of Na^+ co-doped $CaTiO_3$:Eu^{3+} photocatalysts for methylene blue degradation, Ceram. Int. 46 (2020) 12111–12119, https://doi.org/10.1016/j.ceramint.2020.01.256.
[16] R. Nain, R.K. Dwivedi, Effect of tuning of charge defects by K, Ba, La doping on structural and electrical behaviour of $NaNbO_3$, Mater. Chem. Phys. 306 (2023) 127999, https://doi.org/10.1016/j.matchemphys.2023.127999.
[17] M. Boukriba, F. Sediri, N. Gharbi, Hydrothermal synthesis and electrical properties of $NaNbO_3$, Mater. Res. Bull. 48 (2013) 574–580, https://doi.org/10.1016/j.materresbull.2012.11.046.
[18] R. Nain, R.K. Dwivedi, Synthesis and dielectric behaviour of La and Cr modified $NaNbO_3$ ($x \leq 0.06$), Mater. Today Proc. (2023). https://doi.org/10.1016/j.matpr.2023.06.431.
[19] C.M. Khor, M.M. Khan, M.Y. Khan, A. Khan, M.H. Harunsani, Enhanced photocatalytic activity of La and Zr-codoped $AgNbO_3$ for rhodamine B and methylene blue degradation, J. Saudi Chem. Soc. 26 (2022) 101534, https://doi.org/10.1016/j.jscs.2022.101534.
[20] K.A.M. Ahmed, K. Huang, Formation of Mn_3O_4 nanobelts through the solvothermal process and their photocatalytic property, Arab. J. Chem. 12 (2019) 429–439, https://doi.org/10.1016/j.arabjc.2014.08.014.
[21] K.K. Mishra, V. Sivasubramanian, A.K. Arora, Low-temperature Raman spectroscopic studies in $NaNbO_3$, J. Raman Spectrosc. 42 (2011) 517–521, https://doi.org/10.1002/jrs.2706.
[22] R. Nain, R.K. Dwivedi, Studies on structural, optical and electrical behavior of La and Cr modified $NaNbO_3$ ($x \leq 0.15$), J. Solid State Chem. 329 (2024) 124378, https://doi.org/10.1016/j.jssc.2023.124378.
[23] S. Ji, et al., Synthesis, structure, and piezoelectric properties of ferroelectric and antiferroelectric $NaNbO_3$ nanostructures, CrystEngComm 16 (2014) 7598–7604, https://doi.org/10.1039/C4CE01116C.
[24] M. Jauhari, S.K. Mishra, R. Mittal, S.L. Chaplot, Probing of structural phase transitions in barium titanate modified sodium niobate using Raman scattering, J. Raman Spectrosc. 50 (2019) 1177–1185, https://doi.org/10.1002/jrs.5618.
[25] Y. Hsiao, Y.-H. Chang, T. Fang, Y. Chang, Y. Chai, Microstructural, Raman and dielectric properties of $(1-x)NaNbO_3$–$xBiCrO_3$ biphase ceramics, J. Alloys Compd. 430 (2007) 313–319, https://doi.org/10.1016/j.jallcom.2006.05.022.
[26] G. Venkatesh, et al., Construction and investigation on perovskite-type $SrTiO_3$@ reduced graphene oxide hybrid nanocomposite for enhanced photocatalytic performance, Colloids Surfaces A Physicochem. Eng. Asp. 629 (2021) 127523, https://doi.org/10.1016/j.colsurfa.2021.127523.
[27] D. Heger, J. Jirkovský, P. Klán, Aggregation of methylene blue in frozen aqueous solutions studied by absorption spectroscopy, J. Phys. Chem. A 109 (2005) 6702–6709, https://doi.org/10.1021/jp050439j.
[28] A.S. Vig, N. Rani, A. Gupta, O.P. Pandey, Influence of Ca-doped $NaNbO_3$ and its heterojunction with g-C_3N_4 on the photoredox performance, Sol. Energy 185 (2019) 469–479, https://doi.org/10.1016/j.solener.2019.04.088.

[29] F.R. Praxedes, M.A.L. Nobre, P.S. Poon, J. Matos, S. Lanfredi, Nanostructured $K_xNa_{1-x}NbO_3$ hollow spheres as potential materials for the photocatalytic treatment of polluted water, Appl. Catal. B Environ. 298 (2021) 120502, https://doi.org/10.1016/j.apcatb.2021.120502.
[30] N.A. Youssef, S.A. Shaban, F.A. Ibrahim, A.S. Mahmoud, Degradation of methyl orange using Fenton catalytic reaction, Egypt. J. Pet. 0–4 (2016), https://doi.org/10.1016/j.ejpe.2015.07.017.
[31] H. Xu, et al., Synthesis , characterization and photocatalytic activity of $NaNbO_3$/ZnO heterojunction photocatalysts, J. Alloys Compd. 509 (2011) 9157–9163, https://doi.org/10.1016/j.jallcom.2011.06.100.
[32] U. Farooq, R. Phul, S.M. Alshehri, J. Ahmed, T. Ahmad, Electrocatalytic and enhanced photocatalytic applications of sodium niobate nanoparticles developed by citrate precursor route, Sci. Rep. 9 (2019) 1–18, https://doi.org/10.1038/s41598-019-40745-w.
[33] N.X.P.S. Database, NIST Standard Reference Database Number 20, National Institute of Standards and Technology, Gaithersburg MD, 20899, 2000.
[34] L. Li, et al., Synthesis of CoO/$KNbO_3$ p-n heterojunction photocatalysts with enhanced H_2 production, Catal. Letters 151 (2021) 755–763, https://doi.org/10.1007/s10562-020-03328-3.
[35] P. Hao, et al., Electrospun single crystalline fork-like $K_2V_8O_{21}$ as high-performance cathode materials for lithium-ion batteries, Front. Chem. 6 (2018) 1–9, https://doi.org/10.3389/fchem.2018.00195.
[36] D. Yuan, et al., Enhanced thermoelectric performance of c-axis-oriented epitaxial Ba-doped BiCuSeO thin films, Nanoscale Res. Lett. 13 (2018), https://doi.org/10.1186/s11671-018-2752-6.
[37] S.R. Sanivarapu, J.B. Lawrence, G. Sreedhar, Role of surface oxygen vacancies and lanthanide contraction phenomenon of $ln(OH)_3$ (ln = La, Pr, and Nd) in sulfide-mediated photoelectrochemical water splitting, ACS Omega 3 (2018) 6267–6278, https://doi.org/10.1021/acsomega.8b00429.
[38] K.D. Singh, R. Pandit, R.S.C. Kumar, Solid State Sci. 3 (2018).
[39] R. Kumar, K.D. Singh, R. Kumar, Effect of Sr substitution on structural properties of $LaCrO_3$ perovskite, J. Mater. Sci. Mater. Electron. 33 (2022) 12039–12052, https://doi.org/10.1007/s10854-022-08164-2.
[40] A. Prudnikava, et al., Systematic study of niobium thermal treatments for superconducting radio frequency cavities employing x-ray photoelectron spectroscopy, Supercond. Sci. Technol. 35 (2022) 065019, https://doi.org/10.1088/1361-6668/ac6a85.
[41] L. Hao, et al., Achieving a high dielectric tunability in strain-engineered tetragonal $K_{0.5}Na_{0.5}NbO_3$ films, npj Comput. Mater. 7 (2021) 1–9, https://doi.org/10.1038/s41524-021-00528-2.
[42] A.V. Kovalevsky, et al., Designing strontium titanate-based thermoelectrics: insight into defect chemistry mechanisms, J. Mater. Chem. A 5 (2017) 3909–3922, https://doi.org/10.1039/C6TA09860F.
[43] D.Q. Liu, et al., Effect of Nb doping on microstructures and thermoelectric properties of $SrTiO_3$ ceramics, Chinese Phys. B 27 (2018), https://doi.org/10.1088/1674-1056/27/4/047205.
[44] J.B. Li, et al., Broadening the temperature range for high thermoelectric performance of bulk polycrystalline strontium titanate by controlling the electronic transport properties, J. Mater. Chem. C 6 (2018) 7594–7603, https://doi.org/10.1039/C8TC02130A.
[45] B. Yang, et al., Enhanced photocatalytic activity of perovskite $NaNbO_3$ by oxygen vacancy engineering, Phys. Chem. Chem. Phys. 21 (2019) 11697–11704, https://doi.org/10.1039/C9CP01763A.
[46] M.F. Ehsan, et al., $CoFe_2O_4$ decorated g-C_3N_4 nanosheets: new insights into superoxide anion mediated photomineralization of methylene blue, J. Environ. Chem. Eng. 8 (2020) 104556, https://doi.org/10.1016/j.jece.2020.104556.
[47] N.A.M. Barakat, G.M.K. Tolba, K.A. Khalil, Methylene blue dye as photosensitizer for scavenger-less water photo splitting: new insight in green hydrogen technology, Polymers 14 (2022) 1–15, https://doi.org/10.3390/polym14030523.
[48] O.V. Nkwachukwu, et al., Photoelectrochemical degradation of organic pollutants on a La^{3+} doped $BiFeO_3$ perovskite, Catalysts 11 (2021), https://doi.org/10.3390/catal11091069.
[49] Y. Cui, S.M. Goldup, S. Dunn, RSC Advances Photodegradation of Rhodamine B over Ag modi fi ed ferroelectric $BaTiO_3$ under simulated solar light : pathways and mechanism, RSC Adv. 5 (2015) 30372–30379, https://doi.org/10.1039/C5RA00798D.
[50] G. Naresh, T.K. Mandal, Efficient COD removal coinciding with dye decoloration by five-layer aurivillius perovskites under sunlight-irradiation, ACS Sustain. Chem. Eng. 3 (2015) 2900–2908, https://doi.org/10.1021/acssuschemeng.5b00853.
[51] A. Singh Vig, N. Rani, A. Gupta, O.P. Pandey, Influence of Ca-doped $NaNbO_3$ and its heterojunction with g-C_3N_4 on the photoredox performance, Sol. Energy 185 (2019) 469–479, https://doi.org/10.1016/j.solener.2019.04.088.
[52] A. Ajmal, I. Majeed, R.N. Malik, H. Idriss, M.A. Nadeem, Principles and mechanisms of photocatalytic dye degradation on TiO_2 based photocatalysts: a comparative overview, RSC Adv. 4 (2014) 37003–37026, https://doi.org/10.1039/C4RA06658H.